J. Fluid Mech. (1977), *vol.* 83, *part* 2, *pp.* 249–272
Printed in Great Britain

Computational and experimental investigations of two-dimensional nonlinear peristaltic flows

By THOMAS D. BROWN

Department of Orthopaedic Surgery, University of Pittsburgh, Pennsylvania 15261

AND TIN-KAN HUNG

Departments of Civil Engineering and Neurosurgery, University of Pittsburgh, Pennsylvania 15261

(Received 3 February 1977)

An implicit finite-difference technique employing orthogonal curvilinear co-ordinates is used to solve the Navier–Stokes equations for peristaltic flows in which both the wall-wave curvature and the Reynolds number are finite (§ 2). The numerical solutions agree closely with experimental flow visualizations. The kinematic characteristics of both extensible and inextensible walls (§ 3) are found to have a distinct influence on the flow processes only near the wall. Without vorticity, peristaltic flow observed from a reference frame moving with the wave will be equivalent to steady potential flow through a stationary wavy channel of similar geometry (§ 4). Solutions for steady viscous flow (§ 5) are obtained from simulation of unsteady flow processes beginning from an initial condition of potential peristaltic flow. For nonlinear flows due to a single peristaltic wave of dilatation, the highest stresses and energy exchange rates (§ 6) occur along the wall and in two instantaneous stagnation regions in the bolus core. A series of computations for periodic wave trains reveals that increasing the Reynolds number from 2·3 to 251 yields a modest augmentation in the ratio of flow rate to Reynolds number but induces a much greater increase in the shear stress (§ 7.1). The transport effectiveness is markedly reduced for pumping against a mild adverse pressure drop (§ 7.2). Increasing the wave amplitude will lead to the development of travelling vortices within the core region of the peristaltic flow (§ 7.3).

1. Introduction

Periodic and sporadic pumping of fluids or fluid–solid mixtures through muscular tubes by means of peristaltic waves is a widely employed biological transport mechanism. Examples include the passage of urine from kidneys to bladder, the movement of chyme in the gastro-intestinal tract, and the ejection of semen from male reproductive organs. Many of the essential fluid-mechanical characteristics of peristalsis have been elucidated by engineering analyses. These studies, which are reviewed by Jaffrin & Shapiro (1971), have focused almost exclusively upon cases for which the ratio of wave amplitude to wavelength is zero or very small (implying negligible wall curvature) and/or for which inertial effects are insignificant.

When the complex interaction of the moving wall with the flow field leads to highly curvilinear fluid motion at finite Reynolds numbers, it becomes necessary to undertake

nonlinear analysis. The first study of peristaltic flow which included small nonlinear effects was performed by Fung & Yih (1968) for a two-dimensional channel with finite amplitude-to-wavelength ratio. Their analysis, which was based upon perturbations of the ratio of wave amplitude to mean channel width, yielded a simplified solution for the case of free pumping (i.e. no flow if the wall motion stops). A similar analysis was reported by Yin & Fung (1971) for an axisymmetric case along with experimental verification of analytical results for one-wall peristalsis in a two-dimensional channel. Further extension was provided in a paper by Mittra & Prasad (1973), which included the effects of thin elastic or viscoelastic channel walls and a uniform pressure gradient.

The early linear solution of Shapiro, Jaffrin & Weinberg (1969) was modified by Jaffrin (1973), who performed perturbation analyses to examine both the effect of long but finite wavelengths at zero Reynolds number and the effect of small but finite Reynolds numbers at infinite wavelength. Comparison with Eckstein's (1970) experimental data showed reasonable agreement of the pressure/flow relationships within the range of validity of the perturbation analyses. Tong & Vawter (1972) employed a finite-element method to study peristaltic flow. Their creeping-flow formulation was applicable to axisymmetric peristaltic flow with arbitrary wave geometry.

The authors have been engaged in studies of nonlinear peristaltic flows from both experimental and computational viewpoints. In a previous paper (Hung & Brown 1976), a technique for the generation and visualization of two-dimensional peristaltic flows was presented. Several phenomena encountered in linear peristaltic flows (such as trapping and retrograde flow) were demonstrated to occur in the nonlinear regime as well. It was further shown that solid particles can be effectively transported by peristalsis. The effects of wave amplitude, the ratio of particle size to channel width, the Reynolds number, the gravitational force and asymmetry on the particle transport were studied. In the present paper, the results of computational simulations of nonlinear peristaltic flows will be discussed. Close agreement is observed in all cases between experimental flow visualizations and the numerical results.

The effects of variations in Reynolds number over three orders of magnitude are studied in one series of computations, while the effects of extreme wall curvature (i.e. large wave amplitude) are treated in another. Of particular interest is the stress field resulting from the wall motion, since peristaltic roller pumps operating in the nonlinear regime are commonly employed in surgical heart–lung bypass procedures. Jaffrin & Meginniss (1971), who adapted the creeping-flow solution of Shapiro *et al.* (1969) to the geometry of a roller pump, have shown that shear stresses in excess of those known to induce damage to red blood cells can be developed in the neck sections of highly occluded roller pumps. Evidence has since accumulated that serious damage to platelets (the blood elements responsible for the clotting mechanism) occurs at much lower stress levels (Brown *et al.* 1975; Hung *et al.* 1976). Detailed characteristics of the stress field and of the patterns of mechanical energy transfer and balance are discussed in this paper for a train of waves of contraction and dilatation. It is found that the shear stress developed along the peristaltic wall increases dramatically with Reynolds number. Flow and stress field results for single nonlinear waves of contraction will be the subject of a subsequent paper.

2. Computational and experimental method

The numerical procedure is based upon an implicit finite-difference solution of the governing Navier–Stokes and continuity equations, which in orthogonal curvilinear co-ordinates (α, β) take the respective forms

$$\begin{aligned}\frac{\partial U}{\partial T}+\frac{U}{h_1}\frac{\partial U}{\partial \alpha}+\frac{V}{h_2}\frac{\partial U}{\partial \beta}+\frac{UV}{h_1h_2}\frac{\partial h_1}{\partial \beta}-\frac{V^2}{h_1h_2}\frac{\partial h_2}{\partial \alpha}&=-\frac{1}{h_1}\frac{\partial P}{\partial \alpha}\\ +\frac{1}{\mathscr{R}}\left\{\frac{1}{h_1h_2}\left[\frac{\partial}{\partial \alpha}\left(\frac{h_2}{h_1}\frac{\partial U}{\partial \alpha}\right)+\frac{\partial}{\partial \beta}\left(\frac{h_1}{h_2}\frac{\partial U}{\partial \beta}\right)\right]+\frac{2}{h_1}\frac{\partial V}{\partial \beta}\frac{\partial}{\partial \alpha}\left(\frac{1}{h_2}\right)\right.\\ -\frac{2}{h_2}\frac{\partial V}{\partial \alpha}\frac{\partial}{\partial \beta}\left(\frac{1}{h_1}\right)+U\left[\frac{1}{h_1}\frac{\partial}{\partial \alpha}\left(\frac{1}{h_1h_2}\frac{\partial h_2}{\partial \alpha}\right)+\frac{1}{h_2}\frac{\partial}{\partial \beta}\left(\frac{1}{h_1h_2}\frac{\partial h_1}{\partial \beta}\right)\right]\\ \left.+V\left[\frac{1}{h_1}\frac{\partial}{\partial \alpha}\left(\frac{1}{h_1h_2}\frac{\partial h_1}{\partial \beta}\right)-\frac{1}{h_2}\frac{\partial}{\partial \beta}\left(\frac{1}{h_1h_2}\frac{\partial h_2}{\partial \alpha}\right)\right]\right\},\end{aligned} \tag{1}$$

$$\begin{aligned}\frac{\partial V}{\partial T}+\frac{U}{h_1}\frac{\partial V}{\partial \alpha}+\frac{V}{h_2}\frac{\partial V}{\partial \beta}+\frac{UV}{h_1h_2}\frac{\partial h_2}{\partial \alpha}-\frac{U^2}{h_1h_2}\frac{\partial h_1}{\partial \beta}&=-\frac{1}{h_2}\frac{\partial P}{\partial \beta}\\ +\frac{1}{\mathscr{R}}\left\{\frac{1}{h_1h_2}\left[\frac{\partial}{\partial \alpha}\left(\frac{h_2}{h_1}\frac{\partial V}{\partial \alpha}\right)+\frac{\partial}{\partial \beta}\left(\frac{h_1}{h_2}\frac{\partial V}{\partial \beta}\right)\right]+\frac{2}{h_2}\frac{\partial U}{\partial \alpha}\frac{\partial}{\partial \beta}\left(\frac{1}{h_1}\right)\right.\\ -\frac{2}{h_1}\frac{\partial U}{\partial \beta}\frac{\partial}{\partial \alpha}\left(\frac{1}{h_2}\right)+U\left[\frac{1}{h_2}\frac{\partial}{\partial \beta}\left(\frac{1}{h_1h_2}\frac{\partial h_2}{\partial \alpha}\right)-\frac{1}{h_1}\frac{\partial}{\partial \alpha}\left(\frac{1}{h_1h_2}\frac{\partial h_1}{\partial \beta}\right)\right]\\ \left.+V\left[\frac{1}{h_2}\frac{\partial}{\partial \beta}\left(\frac{1}{h_1h_2}\frac{\partial h_1}{\partial \beta}\right)+\frac{1}{h_1}\frac{\partial}{\partial \alpha}\left(\frac{1}{h_1h_2}\frac{\partial h_2}{\partial \beta}\right)\right]\right\}\end{aligned} \tag{2}$$

and

$$\frac{\partial}{\partial \alpha}(h_2U)+\frac{\partial}{\partial \beta}(h_1V)=0. \tag{3}$$

In these equations, U and V denote the dimensionless velocity components in the α and β (tangential and normal) directions, P denotes the dimensionless pressure, T the time, h_1 and h_2 the metrical coefficients, and $\mathscr{R}$ the Reynolds number $\rho cA/\mu$ (A being the wave amplitude, ρ the density and μ the dynamic viscosity; see figure 1*a*). The reference quantities by which the dimensionless variables (U, V), P and T must be multiplied to obtain their dimensional equivalents are, respectively, c, ρc^2 and A/c. Also, the equations of motion are based on a moving co-ordinate system translating longitudinally at a constant speed c.

For peristaltic flow due to the propagation of a wall wave form $y = g(x)$, the flow region is time invariant in a co-ordinate system (x^*, y^*) which translates at a velocity equal to the wave speed. One can generate an orthogonal curvilinear co-ordinate system which is boundary fitted to the moving-frame peristaltic wall ($y^* = g(x^*)$) by solving the inverse Laplace equations

$$\partial^2x^*/\partial\alpha^2+\partial^2x^*/\partial\beta^2=0 \tag{4}$$

and

$$\partial^2y^*/\partial\alpha^2+\partial^2y^*/\partial\beta^2=0. \tag{5}$$

The boundary conditions along the wall for the value of β and the normal derivative of α are

$$\beta|_{\text{wall}}=\text{constant} \tag{6}$$

and

$$[\partial\alpha/\partial n]_{\text{wall}}=0. \tag{7}$$

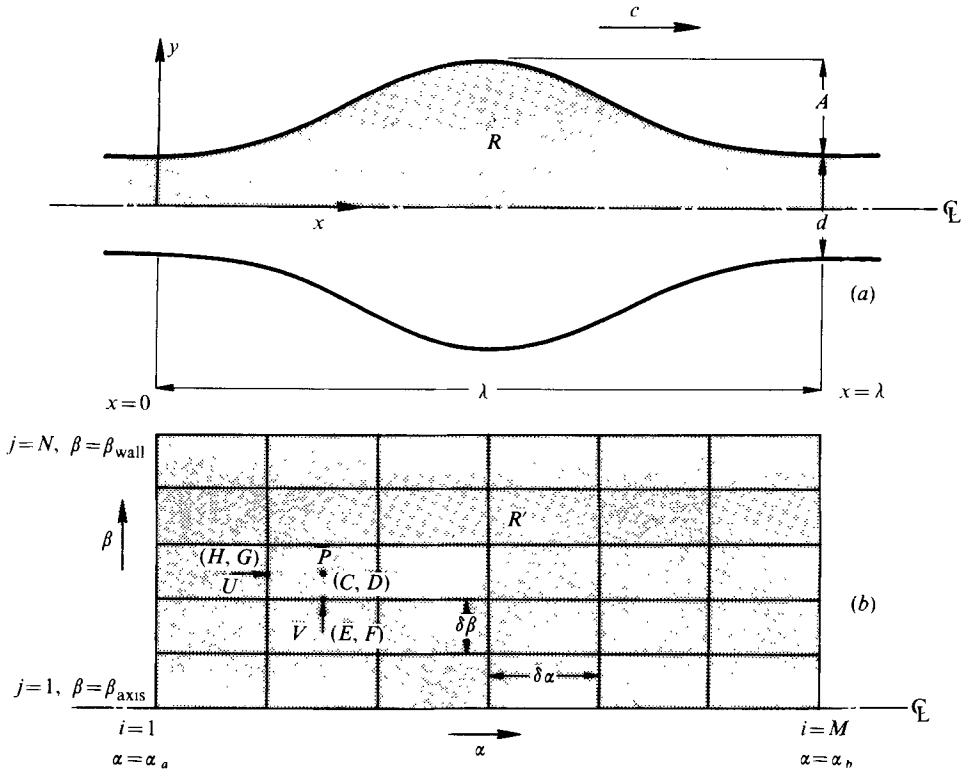

FIGURE 1. (*a*) Definition sketch of the physical region R.
(*b*) Mesh structure in the transformed space R'.

Boundary conditions for α and β at the channel inlet and outlet are selected according to the physical flow characteristics. For a repetitive peristaltic wave train, $\partial\alpha/\partial y$ vanishes at the periodic ends although the difference in α (i.e. $\alpha_a - \alpha_b$, referring to figure 1) is not known. However, $\alpha_a - \alpha_b$ is uniquely determined from the difference in β between the centre-line and the wall. A new dual iterative procedure has been developed to solve (4)–(7) and find $\alpha_a - \alpha_b$ (Hung & Brown 1977). When $\partial a/\partial y$ is non-zero at sections a and b, the mesh can be generated by the much simpler method of Thom & Apelt (1961, p. 44). Figure 2 shows the Laplace solution for α and β used for the present mesh structure. A detailed description of the numerical method has been reported elsewhere (Hung & Brown 1977; Brown 1976). Since the wall boundary conditions (free-slip and impermeability) (6) and (7) can apply equally to a travelling wave of geometry $y_{\text{wall}} = g(x_{\text{wall}} - ct)$, it will be observed that an identical flow pattern exists for a potential peristaltic flow viewed in the moving (steady) reference frame. Clearly, however, the assumption of a free-slip boundary condition remains contradictory to physical reality.

As will be discussed in § 3, potential peristaltic flow is of interest as an idealized limiting case of high Reynolds number ($\mathscr{R}$) peristalsis. A vanishingly thin wall boundary layer is to be expected physically for extremely large values of $\mathscr{R}$. The potential-flow solution calculated in this study provides also an admissible initial condition from which to simulate the viscous flow development using (1)–(3), in

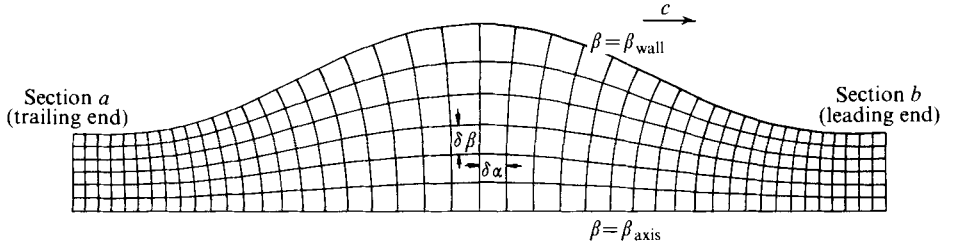

FIGURE 2. Potential-flow net and orthogonal curvilinear co-ordinate system for a single peristaltic bolus.

which the (α, β) co-ordinates become rectilinear. Three pairs of metrical coefficients, (C, D), (E, F) and(H, G), corresponding to the respective points of evaluation of (h_1, h_2) were evaluated and stored in the computer memory. Following the method of Hung (1970), we define values of the flow variables U, V and P for a given mesh cell as indicated in figure 1 (*b*).

From momentum balances at $T = (n+\frac{1}{2})\delta T$ (i.e. forward in time one-half of the discretized time step), one obtains the velocity components at the next time step from finite-difference equations of the form

$$U_{i,j}^{n+1} = \delta T\left[\xi_{i,j} - \left(\frac{1}{h_1 \delta\alpha}\right)(P_{i,j}^{n+\frac{1}{2}} - P_{i-1,j}^{n+\frac{1}{2}})\right]. \tag{8}$$

In this equation, the subscripts designate the spatial mesh indices, while the superscripts refer to the time index. To facilitate the computer coding, $U_{i,j}$ is taken to be one-half mesh length upstream from $P_{i,j}$, and $V_{i,j}$ is taken to be one-half mesh length laterally from $P_{i,j}$ (refer to figure 1 *b*). The symbol $\xi_{i,j}$ denotes a collection of convective and diffusive terms, as well as part of the local acceleration term.

The pressure at the cell centre is obtained from a mass balance:

$$P_{i,j}^{n+\frac{1}{2}} = \left[\frac{\zeta_1}{(\delta\alpha)^2} + \frac{\zeta_2}{(\delta\beta)^2}\right]^{-1}\left[A_{i,j} + \frac{1}{(\delta\alpha)^2}(\gamma_1 P_{i+1,j}^{n+\frac{1}{2}} + \gamma_2 P_{i-1,j}^{n+\frac{1}{2}}) + \frac{1}{(\delta\beta)^2}(\gamma_3 P_{i,j+1}^{n+\frac{1}{2}} + \gamma_4 P_{i,j-1}^{n+\frac{1}{2}})\right]. \tag{9}$$

In this equation, the ζ's and γ's are geometrical factors involving only combinations of the metrical coefficients; $A_{i,j}$ denotes a lengthy collection of terms involving ξ and its β-direction counterpart. The first velocity approximation of this method corresponds to that obtained by the marker-and-cell (MAC) method (Harlow & Welch 1965).

While the boundary condition along the peristaltic wall is uniquely determined from no-slip considerations, the upstream and downstream boundary conditions may be specified in terms of either velocity or pressure distributions. If the pressure drop $P_b - P_a$ between the leading and trailing sections b and a is chosen to be the independent variable, it becomes convenient to characterize the flow in terms of the Kármán number

$$\mathscr{K} = (P_b - P_a)\rho A^2/\mu^2. \tag{10}$$

This transformation is accomplished by setting

$$U' = U\mathscr{R}, \quad V' = V\mathscr{R}, \quad P' = P\mathscr{R}^2 = p\rho A^2/\mu^2. \tag{11a–c}$$

When (11) is introduced into (1)–(3), the Reynolds number no longer appears explicitly, as the velocity is expressed in the form of a Reynolds number (Hung 1970). After dropping the primes on these variables (i.e. $U = U'$ etc.), the new dimensionless form of the Navier–Stokes equations (1)–(3) remains unchanged except that the factor $1/\mathscr{R}$ is replaced by 1.

For a wall whose elements move transversely in the fixed co-ordinates (i.e. in the y direction) but not longitudinally (i.e. in the x direction), the boundary conditions in the moving co-ordinates (i.e. the tangential and normal velocity components at the wall) become

$$U = -\frac{cA}{\mu}\sec\left[\tan^{-1}\left(\frac{dy^*}{dx^*}\right)\right], \quad V = 0. \tag{12a,b}$$

A perturbation will be added to the above expression for U when the wall is inextensible. Taylor's (1951) method can be used if the peristalsis is a continuous train of waves.

Starting with the velocity and pressure fields of potential peristaltic flow, simulation of the transition to steady viscous flow is begun by assuming that the initially inviscid fluid suddenly acquires finite viscosity or equivalently that the boundary-layer effect is included as time advances. Under the corresponding instantaneous initial change in the wall boundary conditions (from free slip to no slip) and in the inlet and outlet boundary conditions (from a driving net potential difference to a driving pressure difference or Kármán number), an implicit iterative procedure is used to obtain solutions of (1)–(3) at successive time steps until an asymptotically steady viscous flow condition is attained. Unlike the famous MAC technique (Harlow & Welch 1965; Welch *et al.* 1966), the nonlinear effects are simulated here by performing several iterations of the velocity field at each time increment, until a relative velocity convergence criterion is satisfied. The pressure field at $(n+\frac{1}{2})\,\delta T$ is recalculated after each intermediate velocity iteration, on the basis of a temporally interpolated velocity field. Details of the iterative procedure and considerations relevant to the selection of convergence criteria are reported in Hung & Brown (1977) and in Brown (1976).

Low Reynolds number peristaltic flows were produced experimentally between two flexible acetate walls suspended vertically in a glycerine-filled towing tank. Two pairs of horizontal wavy channel-section rails, affixed to the towing-tank carriage, were made to mesh with rollers mounted on the ends of vertical Plexiglas ribs, which in turn were attached periodically to each acetate wall. As the rails were towed horizontally by the carriage, the rollers, and therefore the ribs, together with the tethered flexible walls, were constrained to move horizontally so as to follow the shape of the moving rails, thus generating peristaltic waves. Flow visualization was facilitated by fine air bubbles which were generated when the glycerine was pumped from storage drums into the towing tank. The construction and operation of the experimental apparatus were fully discussed in a previous paper (Hung & Brown 1976).

3. Kinematics of the wall and boundary conditions

We consider first the flow due to a single peristaltic wave of dilation propagating along the walls of an otherwise uniform channel. Although Tong & Vawter (1972) reported a finite-element creeping-flow solution with large A/λ for a periodic train of sinusoidal expansion waves separated by straight-wall segments, the case of a solitary peristaltic bolus has not been studied.

Let the single wall wave be prescribed by

$$y = y^* = \begin{cases} \frac{1}{2}d + \frac{1}{2}A[1 + \sin(2\pi x^*/\lambda - \frac{1}{2}\pi)] & \text{for} \quad 0 < x^* < \lambda, \qquad (13a) \\ \frac{1}{2}d \quad \text{for} \quad x^* < 0, \quad x^* > \lambda, \qquad (13b) \end{cases}$$

where d is the distance between the undisturbed parallel walls.

Boundary conditions at the wall are not uniquely determined by this wave geometry; in addition, the deformation characteristics of the wall itself must be specified in order to evaluate the tangential motion of the wall elements. The wall velocity boundary conditions [equations (12)] can be readily obtained by differentiating (13) with respect to time when the wall elements are constrained to move only transversely. If instead the wall is taken to be inextensible, longitudinal as well as lateral wall-element motion ensues.

For a solitary peristaltic wave, the tangential velocity of a given wall element is not constant in the moving reference frame when the wall is tethered behind the trailing edge. Hence the analysis of Taylor is inapplicable, and instead it becomes necessary to calculate the wall-element velocities in the fixed reference frame. The arc length S_i along the wall from the point of tethering (upstream of the trailing edge) to any given point (x_i, y_i) on the wavy wall is constant, and can be written as

$$S_i = \int_0^{x_i^*} [1 + (dy^*/dx^*)^2]^{\frac{1}{2}}\, dx^* + ct, \qquad (14)$$

where ct is the distance the wave has travelled in the time $t\ (= n\,\delta t)$ since the trailing edge and the reference (tethering) point were coincident. Setting

$$\theta = \frac{2\pi x^*}{\lambda} - \frac{\pi}{2} = \frac{2\pi}{\lambda}(x - ct) - \frac{\pi}{2}, \qquad (15)$$

one obtains

$$\frac{S_i}{\lambda} - n\,\delta(ct/\lambda) = \frac{1}{2\pi}\int_{\frac{1}{2}\pi}^{\theta_i} \left(1 + \frac{\pi^2 A^2}{\lambda^2}\cos^2\theta\right)^{\frac{1}{2}} d\theta. \qquad (16)$$

Numerical integration of (16) is necessary to determine the velocity components, which in terms of θ become

$$\frac{u^*}{c} = \frac{1}{2\pi}\frac{d\theta}{d(ct/\lambda)} = f_1\left(\frac{A}{\lambda}, \theta\right) - 1 \qquad (17)$$

and

$$\frac{v^*}{c} = \frac{A}{2\lambda}\cos\left[\frac{d\theta}{d(ct/\lambda)}\right] = \frac{\pi A}{\lambda}\cos\frac{u^*}{c} = f_2\left(\frac{A}{\lambda}, \theta\right), \qquad (18)$$

respectively. Because of the inextensibility of the flexible wall, u and v are seen to be linearly related to c, and the velocity distributions u^*/c and v^*/c in the moving frame depend solely on the wave form of the peristalsis.

The quantity $d\theta/d(ct/\lambda)$ can be calculated as follows. For a given wall element, S_i is constant, and at a prescribed time $n\delta(ct/\lambda)$ the upper limit θ_i^n (where the superscript n indicates the time increment number) can be calculated from (16) by an iterative procedure. When the time is increased to $(n+1)\,\delta(ct/\lambda)$, another value of the upper limit, θ_i^{n+1}, is calculated for the same S_i. Thus, if $\delta(ct/\lambda)$ is small, one can obtain the longitudinal velocity component from

$$\frac{u^*}{c} = \frac{1}{2\pi}\frac{(\theta_i^{n+1} - \theta_i^n)}{\delta(ct/\lambda)}. \qquad (19)$$

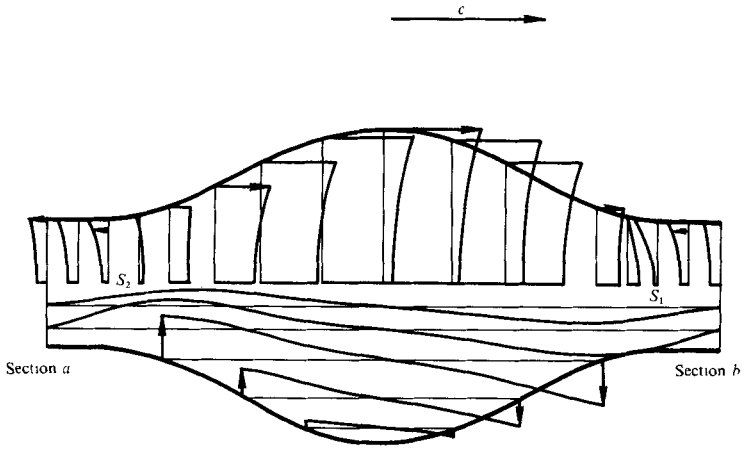

FIGURE 3. Fixed-frame longitudinal (upper) and lateral (lower) velocity profiles for peristaltic potential flow; $d/\lambda = 0{\cdot}203$, $A/\lambda = 0{\cdot}164$, $\phi_b - \phi_a = 8{\cdot}00$.

Distributions of the fixed-frame velocity components u/c and v/c along the wall obtained in this manner were shown in Hung & Brown (1976) without the detailed numerical procedure. The results reveal that for a single bolus the longitudinal wall velocity component is everywhere positive, and that the distributions of the velocity components are such that wall elements execute a trajectory of shape ~. For the periodic case (Taylor 1951; Negrin, Shack & Lardner 1974), the loop is seen to close to a figure-of-eight because of spatially alternating positive and negative longitudinal velocity components. That is to say, for a train of peristaltic waves each wall element periodically retraces its trajectory in the fixed reference frame, while for an isolated peristaltic wave the elements of a tethered inextensible wall experience a single net longitudinal migration.

4. Potential flows

For peristaltic flow between inextensible walls with $A/\lambda = 0{\cdot}164$ and $d/\lambda = 0{\cdot}208$, a potential-flow solution, resembling physically an impulsively accelerated flow, was first obtained as an initial condition for the simulation of viscous flow. Based upon a free-slip boundary condition at the wall and a symmetry line at the bolus axis, the velocity field was solved iteratively for the potential function using Dirichlet inlet and outlet boundary conditions. A driving difference in potential $\phi_b - \phi_a$ between the two end sections was selected such that in the fixed frame the resultant potential-flow field roughly resembled the experimentally observed viscous flow field. As α and β correspond to the potential and stream functions for an irrotational flow through a stationary wave channel, the aforementioned peristaltic potential flow can be simply obtained by superimposing a uniform backward velocity on the appropriately scaled velocity field for $\nabla^2\alpha$.

Figure 3 shows profiles of the longitudinal and lateral components (u and v) of velocity in the fixed Cartesian co-ordinates for the potential peristaltic flow. These two components will be used for plotting velocity profiles throughout this paper. Two stagnation points are shown along the axis near the leading and trailing ends of the

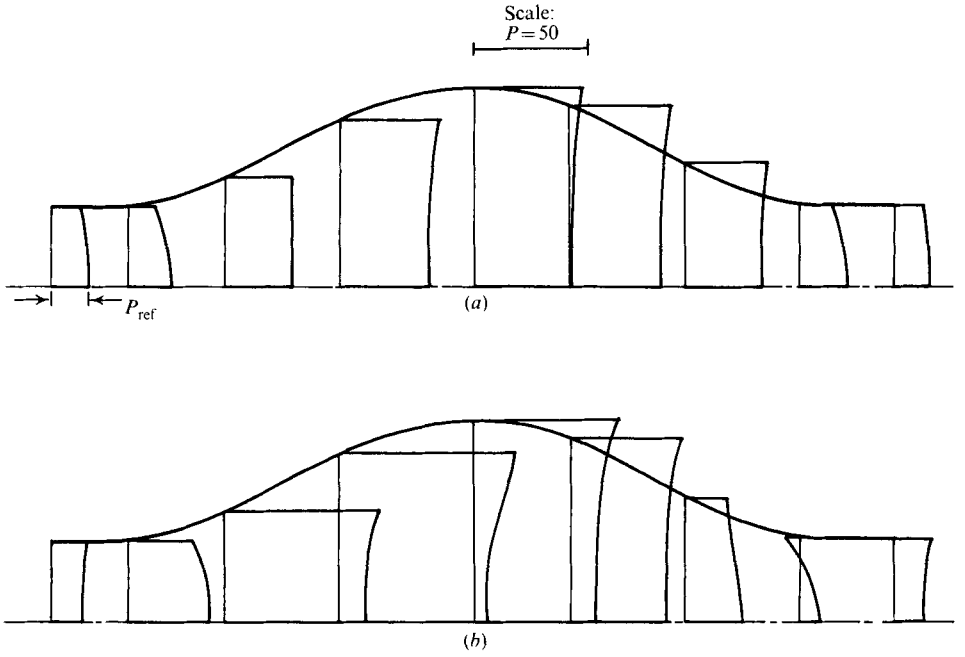

FIGURE 4. Pressure profiles for $A/\lambda = 0{\cdot}164$, $d/\lambda = 0{\cdot}208$. (*a*) Potential flow with $\phi_b - \phi_a = 8{\cdot}00$. (*b*) Viscous flow at $\mathscr{R} = 2{\cdot}36$, $\mathscr{K} = 0$.

bolus, separating the central region of forward flow from two retrograde flow regions. The longitudinal velocity profiles are relatively uniform at each channel section, as is the case in an analysis for the limit of large speed for small wave-amplitude ratios (Hanin 1968). Near the wall, the magnitude of the longitudinal velocity of the potential flow is seen to increase slightly, except at sections near the stagnation points S_1 and S_2. The lateral velocity component becomes significant at those sections where the wall is dilating or contracting rapidly. A region of slightly elevated pressure is found on the wall at the point of maximum channel width (i.e. at $x^* = \frac{1}{2}\lambda$), along with two regions of slightly lowered pressure near the leading and trailing edges of the bolus (see figure 4*a*). Since in the fixed reference frame the flow is unsteady, regions of high pressure do not necessarily coincide with the axial stagnation points. The geometrical symmetry (about the line $x^* = \frac{1}{2}\lambda$) results in equality of pressure at the inlet and the outlet for this idealized potential case.

5. Viscous flows

Keeping zero pressure drop, the viscous flow development shows a continuous alteration of the flow rate until the flow approaches the steady state. The transient discharge and the relative error ϵ_ψ in the numerically integrated discharge past consecutive stations, or equivalently in the stream function along the wall, are plotted in figure 5 for an inextensible wall as well as for an elastic wall. (The former has finite u on the wall while the latter does not.) Because of the prescribed value of $\phi_b - \phi_a$, the temporal-mean discharge of the potential flow at a section in the fixed frame was

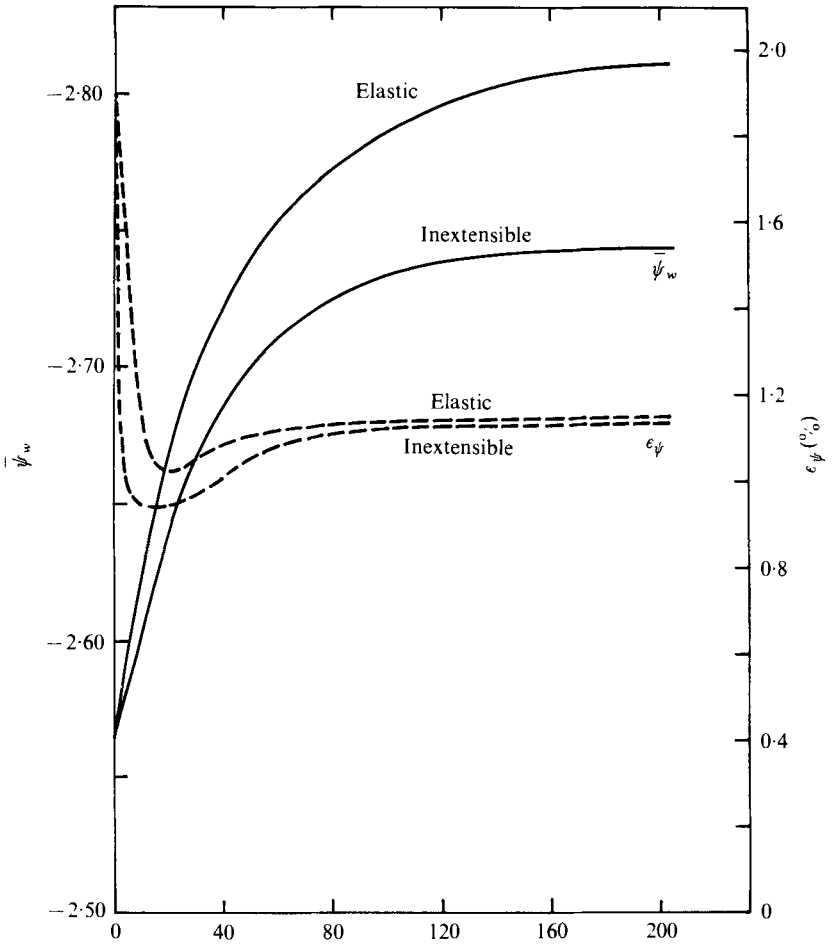

FIGURE 5. Effect of wall inextensibility on viscous discharge. $A/\lambda = 0{\cdot}164$, $d/\lambda = 0{\cdot}208$, $\mathscr{R} = 2{\cdot}36$, $\mathscr{K} = 0$, $\delta T = 0{\cdot}005$, $\phi_b - \phi_a = 8{\cdot}00$.

slightly positive. As the viscous effects developed, the moving-frame discharge became increasingly more negative, indicating that the effect of viscosity was to slow down the net forward flow in the fixed frame. Should the flow rate of the initial potential flow be smaller than that of the steady viscous case, the effect of viscosity would be to increase the net forward flow rate. The discharge for the inextensible wall boundary condition is about 2 % larger than that for the elastic wall boundary condition, a finding which is attributed to the Couette effect of the small forward longitudinal wall velocity in the former case.

At $T = 1{\cdot}00$ ($= 200\,\delta T$), the time rate of change of the average wall stream function had decreased to 1·17 % of its initial value; at this time, the flow was considered to have reached a steady state. Contours of the moving-frame stream function and of the pressure are shown in figure 6. Near the leading and trailing ends of the bolus, the backward velocity in the moving frame increases from the wall to the axis, while at the midsection of the bolus ($x^* = \frac{1}{2}\lambda$) it decreases from the wall to the core. These trends are the opposite of those observed for the potential-flow case.

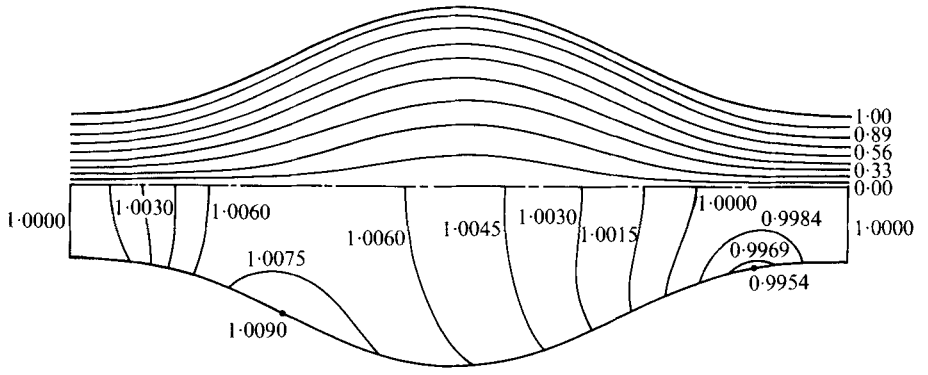

FIGURE 6. Moving-frame streamlines (upper) and pressure contours (lower) for asymptotically steady viscous flow. $A/\lambda = 0{\cdot}164$, $d/\lambda = 0{\cdot}208$, $\mathscr{R} = 2{\cdot}36$, $\mathscr{K} = 0$, $\bar{\psi}_w = -2{\cdot}747$. Values shown for isobars are normalized to a reference pressure $P_{\text{ref}} = 551{\cdot}5$ prescribed on both ends.

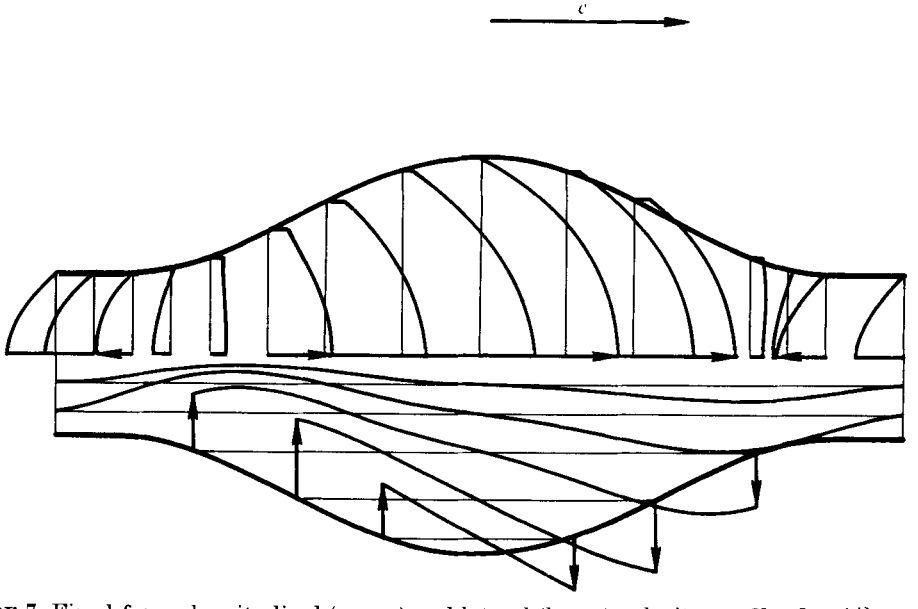

FIGURE 7. Fixed-frame longitudinal (upper) and lateral (lower) velocity profiles for $A/\lambda = 0{\cdot}164$, $d/\lambda = 0{\cdot}208$, $\mathscr{R} = 2{\cdot}36$, $\mathscr{K} = 0$. Inextensible wall boundary condition.

Profiles of the longitudinal and lateral components of velocity viewed from the fixed reference frame are presented in figure 7. Compared with the potential-flow solution (refer to figure 3), the two axial stagnation points S_1 and S_2 have moved closer together for the viscous case, indicating that the region of forward flow has become somewhat smaller. The longitudinal velocity profiles are now found to be roughly parabolic, except near the wall, where they are influenced noticeably by the small forward longitudinal wall velocity component associated with the inextensible wall condition. Along the axis at the midsection ($x^* = \frac{1}{2}\lambda$) the longitudinal velocity is nearly 75 % as great as the wave speed. Should the wave speed be exceeded (as is the case for the large amplitude wave discussed below), two secondary trapping vortices will be observed

in the moving reference frame. The lateral velocity component is dominated by the outward fluid movement in the leading (dilating) half of the bolus and by the inward fluid movement in the trailing (constricting) half. It can be seen that along much of the wavelength, and especially near the midsection, the lateral velocity of the fluid at the wall is somewhat greater for the viscous flow than for the potential one. While the condition of zero normal flux at the wall is the same for both cases, the tangential boundary conditions differ. A large forward tangential velocity is observed along the dilated portion of the wall for the potential flow, while for the viscous no-slip boundary condition this velocity component is zero. Because the tangential velocity of the potential flow has a lateral component that is in the opposite direction to the lateral wall motion, the net lateral velocity for potential flow is somewhat smaller than that for the viscous case.

A comparison between the numerical solution and the experimentally observed flow provides direct evidence of the validity of the computation. As can be seen from the fixed-frame velocity field composite of figure 8 (plate 1), the agreement between computation and experiment is excellent. In the upper half of this figure, the calculated velocity is plotted vectorially at each mesh node; in the lower half, the velocity is represented by light streaks which are time-lapse path lines of fine air bubbles suspended in the fluid (Hung & Brown 1976). The velocity vector (**V**) plot scaling factor and the camera exposure time t_c were chosen such that a given bubble-trace path length can be expressed as $|\mathbf{V}|\,t_c$ if the path-line curvature and the transient flow characteristics in the fixed frame are neglected. Because of the inextensibility of the acetate wall, the bubble traces are seen to have a small forward longitudinal component along both the contracting and the dilating portion of the wall. The spacing between the two axial stagnation points, an instantaneous landmark of the flow, is accurately predicted by the computation. Note that the fluid is not actually stagnant along the wall at the leading and trailing edges of the peristaltic wave since its angular velocity there is non-zero.

Temporal integration of this velocity field reveals that fluid elements moving along the bolus centre-line undergo both forward and retrograde motion. As shown in figure 9, a fluid particle initially ($ct/\lambda = 0$) positioned at the midpoint of a downstream section is first pulled backwards as the wave approaches, passing the leading edge of the wave (trajectory shown by the broken line) at point B. Shortly thereafter ($ct/\lambda = 0{\cdot}14$), the fluid comes to rest, and then moves forwards until $ct/\lambda = 1{\cdot}70$. The trailing edge of the wave passes the fluid element at point C, at which time the fluid element is again found to be moving backwards. This pattern of fluid motion is very similar to that observed experimentally for large solid particles transported along the symmetry axis of a peristaltic flow (Hung & Brown 1976).

The pressure field calculated for asymptotically steady viscous flow displays longitudinal asymmetry, as is shown by the contour plot in the lower half of figure 6. The values indicated for the isobars are normalized to a reference pressure point located at $x^* = y^* = 0$, i.e. along the axis at the trailing edge of the bolus ($P = 1{\cdot}00$). During the pressure iteration [equation (9)], P at this reference point was kept fixed so as to prevent overall drifting of the pressure field in the computational simulation. The point of maximum pressure is found to occur at the wall about midway between the longitudinal symmetry plane of the wall wave ($x^* = \frac{1}{2}\lambda$) and the trailing edge. This high pressure region coincides with the location of maximum contractile velocity of the

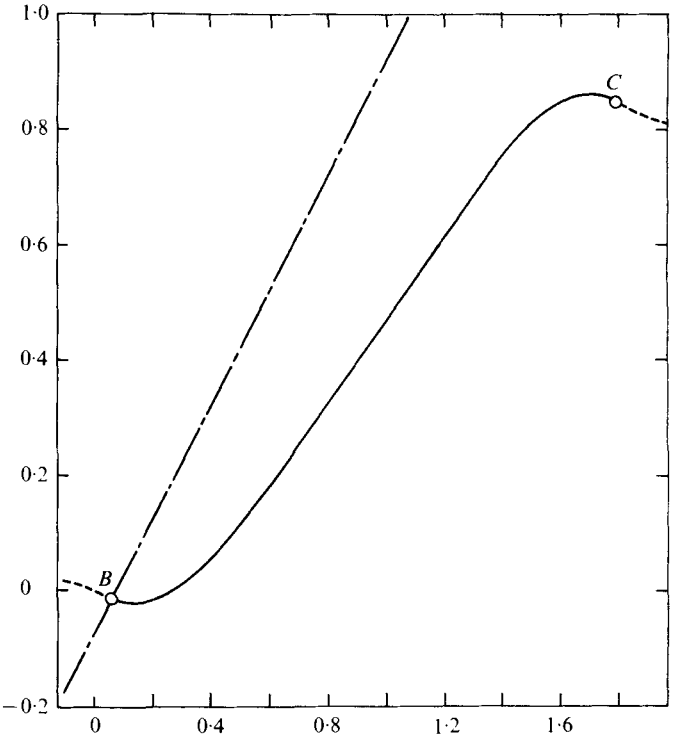

FIGURE 9. Trajectory of fluid elements along bolus centre-line for $A/\lambda = 0{\cdot}164$, $d/\lambda = 0{\cdot}209$, $\mathscr{R} = 2{\cdot}36$, $\mathscr{K} = 0$.

wall. The area of minimum pressure is also located at the wall, but is somewhat nearer to the leading edge than to the point of maximum wall dilatational velocity. The pressure field is also plotted in profile form in the lower half of figure 4 to facilitate comparison with the initial, potential-flow pressure profiles. It can be seen that the pressure field for the viscous solution exhibits greater variation both longitudinally and laterally than is the case for the potential flow.

For a two-dimensional flow, the components of the deviatoric stress tensor in orthogonal curvilinear co-ordinates become

$$\sigma_\alpha = \frac{2\mu}{h_1}\left(\frac{\partial u}{\partial \alpha} + \frac{v}{h_2}\frac{\partial h_1}{\partial \beta}\right), \tag{20a}$$

$$\sigma_\beta = \frac{2\mu}{h_2}\left(\frac{\partial v}{\partial \beta} + \frac{u}{h_1}\frac{\partial h_2}{\partial \alpha}\right) \tag{20b}$$

and

$$\tau_{\alpha\beta} = \mu\left[\frac{h_1}{h_2}\frac{\partial}{\partial \beta}\left(\frac{u}{h_1}\right) + \frac{h_2}{h_1}\frac{\partial}{\partial \alpha}\left(\frac{v}{h_2}\right)\right]. \tag{20c}$$

The normal viscous stress σ_β in the β direction and the shearing stress $\tau_{\alpha\beta}$ are plotted in contour form in figure 10. As a consequence of the equation of continuity, the normal viscous stresses at a point identically sum to zero. The numerical values of σ_x in the

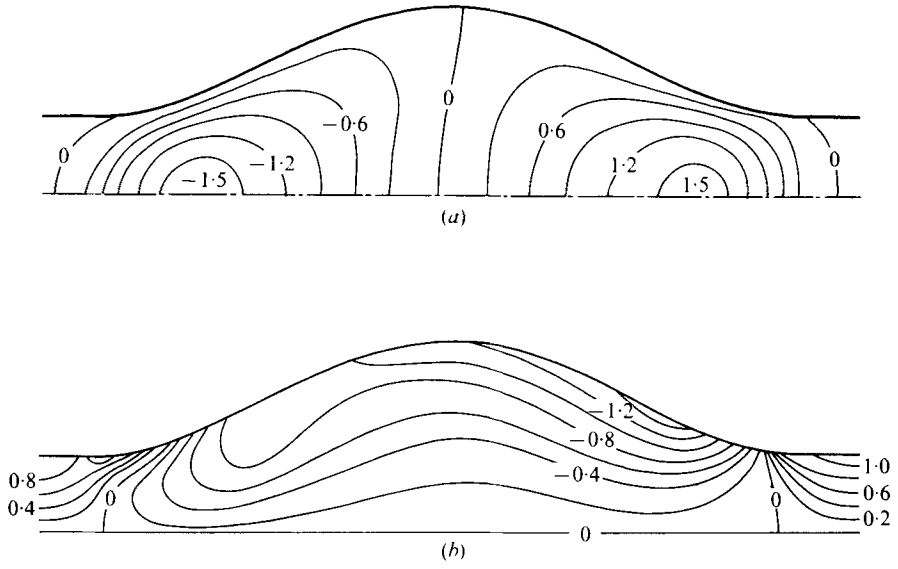

FIGURE 10. (a) Contours of the β-direction normal viscous stress for the flow in figure 8. (b) Contours of the shearing stress.

present calculation are found to be very nearly (average relative error = 0·35 %) equal to $-\sigma_\beta$. Both of the normal viscous stresses are roughly symmetrical about the bolus midsection ($x^* = \frac{1}{2}\lambda$), their magnitudes reaching their maximum values in the stagnation regions along the axis. The magnitude of the spatial variation of the normal viscous stress in this peristaltic flow field is nearly 43 % of the variation observed for the pressure. The shearing stress peaks along the wall, and is somewhat stronger in the dilating segment than in the contracting one.

6. Energy transfer characteristics

The equation of mechanical energy conservation at a point in the flow field for steady incompressible flow in the absence of body forces can be written as

$$(\nabla . \tfrac{1}{2}\rho V^2 \mathbf{V}) + (\nabla . p\mathbf{V}) + [\nabla . (\boldsymbol{\tau} . \mathbf{V})] - (\boldsymbol{\tau} : \nabla \mathbf{V}) = 0. \tag{21}$$

In this equation, the four terms on the left-hand side denote, respectively, the rate of convection of kinetic energy, the rate of work done by pressure, the rate of work done by viscous stresses and the rate of energy dissipation.

To evaluate the various terms in the work/energy relationship, the velocity and pressure in the moving reference frame rather than in the fixed reference frame are employed. Contour plots of the rates of work and of energy convection and dissipation are shown in figure 11. As is to be expected from the small variation in velocity and pressure in the core region of the bolus, relatively little energy interchange takes place there. Areas of complex interaction are identified, however, along the centre-line near the fixed-reference-frame stagnation points S_1 and S_2 (refer to figure 8), as well as along much of the wall. Near the leading stagnation point S_1, the inward convection of kinetic energy from the right and left, due to the longitudinal velocity gradients,

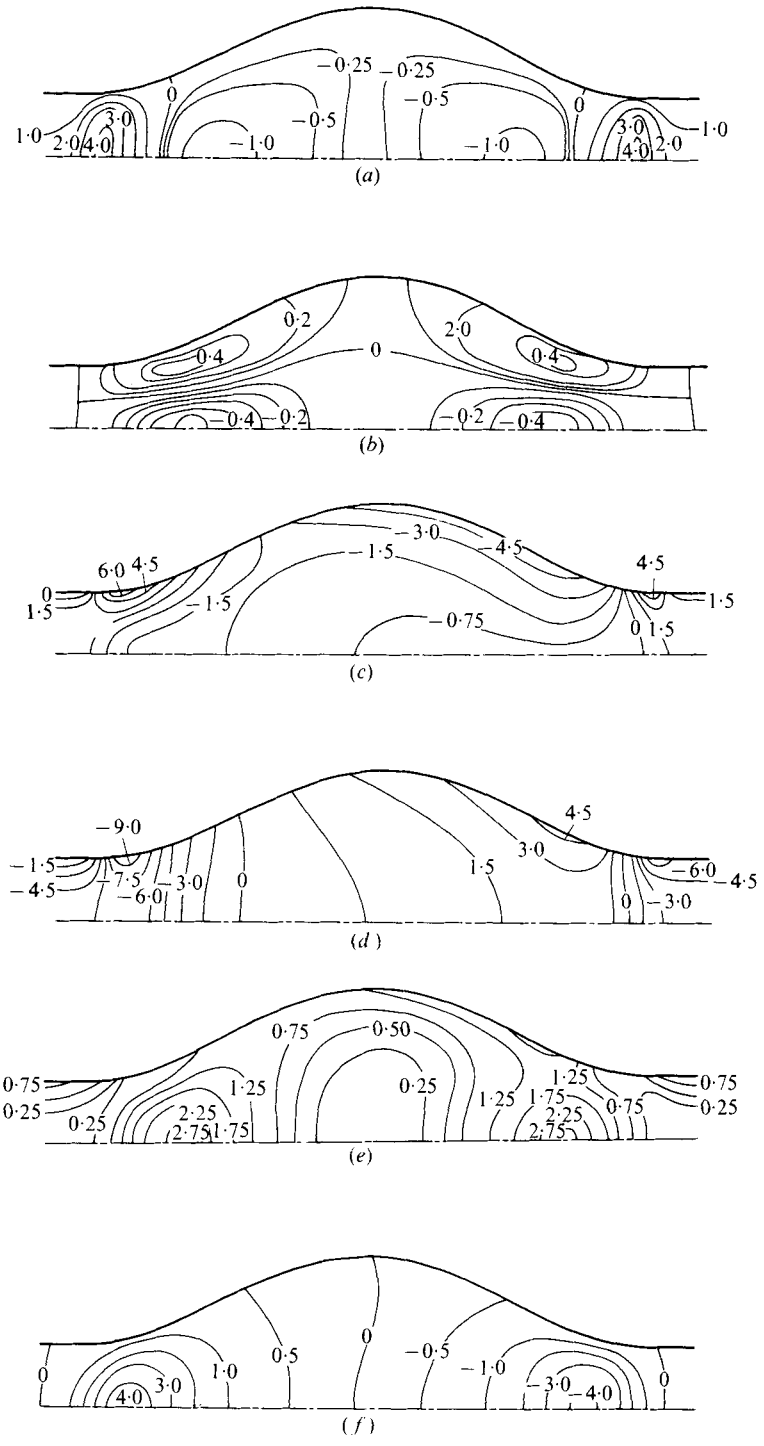

FIGURE 11. (*a*) Rate of working of the α-direction normal viscous stress. (*b*) Rate of working of the β-direction normal viscous stress. (*c*) Rate of working of the shear stress. (*d*) Rate of working of the pressure. (*e*) Local rate of energy dissipation. (*f*) Local rate of convection of kinetic energy.

exceeds the outward convection towards the wall associated with wall dilatation and the lateral velocity gradient. This net rate of kinetic energy influx is balanced primarily by the rate of viscous dissipation and by the rate of work done against the α-direction normal viscous stress. Near the trailing stagnation point S_2, the rates of viscous dissipation and of work done against σ_α are essentially the same as those near the leading stagnation point. Although the magnitudes of the kinetic energy convection rates are also roughly equal, the positive values around S_2 indicate a net efflux of kinetic energy, as opposed to the net influx around S_1. Unlike the dilating segment at S_1, however, the principal rate of energy input near S_2 in the contracting region is provided by the work done by the pressure. Note that the rate of work by σ_β, although maximal in the stagnation regions, is relatively insignificant because of the small lateral variation of the velocity component in the β direction. The rate at which work is done by the normal viscous stress component σ_α in the α direction is

$$\frac{\partial}{\partial \alpha}\left[u\frac{\partial}{\partial h_1}\mu\left(\frac{\partial u}{\partial \alpha}+\frac{v}{h_2}\frac{\partial h_1}{\partial \beta}\right)\right].$$

In the moving co-ordinates, the second term in the parentheses vanishes at the wall, where $v = 0$. For the case of an inextensible wall, $\partial u/\partial \alpha$ is also zero on the wall, resulting in the zero contribution of σ_α to energy transfer there. A finite value of $\partial u/\partial \alpha$ may occur along an extensible wall.

It can be seen that near the wall region the primary exchange of energy is between work done by pressure and that done by shear stress. An area of particularly intense activity is observed at the trailing edge of the curved wall segment, where pressure work associated with active wall contraction supplies energy to the shear field. An area of somewhat less intense exchange is found to be centred near the point of most rapid wall dilatation; here the energy derived from work done by the shear field is expended primarily as pressure work. Should the wall dilation at the leading edge be passive (i.e. pushed by the fluid) rather than actively imposed, one would expect the patterns of local energy interconversion and dissipation to be altered, since energy would be expended in mechanical deformation of the wall and in work done by pressure against the exterior of the channel.

The numerical accuracy of the energy balance, as reflected in the local residue of the sum of the six component terms, was judged to be satisfactory. The average relative local residue was about 2 %, concentrated primarily in regions with high gradients of shear stress and pressure (Brown 1976).

The spatial exchange of energy within the bolus can be further appreciated from the profile plots of the local energy dissipation rate and the local Bernoulli sum shown in figure 12. The combination of the free pumping and periodic end boundary conditions for this flow requires that the Bernoulli sum at the leading-edge section (section 11) equals that at the trailing-edge section (section 1) in the moving reference frame. That is to say, the walls supply energy to the flow field at a rate equal to the total rate of viscous energy dissipation. When the peristaltic wave propagates from left to right, the Bernoulli sum in the moving frame first decreases (sections 11–9), then increases (sections 9–4) (in spite of energy dissipation throughout this region) and finally decreases again back to the value at section 11 because of free pumping. Much of this energy is apparently derived from the active dilatation of the leading half of the wall.

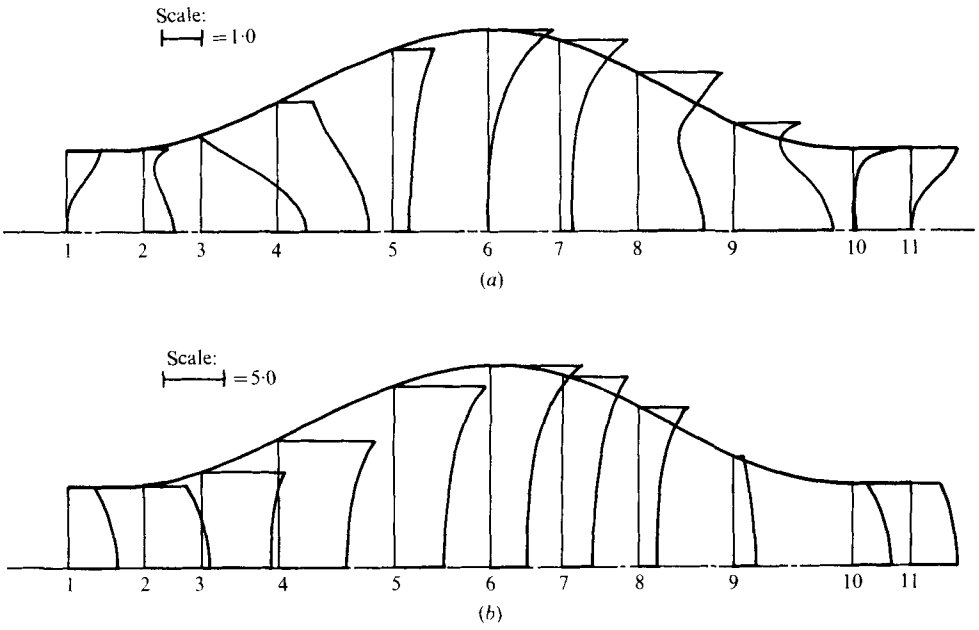

FIGURE 12. Profiles of (*a*) the rate of viscous energy dissipation and (*b*) the variation of the Bernoulli sum for the flow in figure 8.

7. Interaction of fluid inertia and wall curvature effects

To explore the individual and combined effects of fluid inertia and streamline curvature, we now consider the case of a two-dimensional channel along whose walls a periodic train of finite amplitude sinusoidal waves is propagated. The wall is assumed to be extensible and to undergo only transverse motion. That is to say, in the fixed reference frame the longitudinal velocity component at the wall vanishes. Comparison of the numerical solutions for flow under these boundary conditions with those shown in the previous section will indicate the effects of the (spatially variant) longitudinal wall velocity component upon the transport processes.

In this section, three Reynolds numbers ($\rho cA/\mu$ = 2·25, 25·1 and 251) were selected to demonstrate the inertial effects for a periodic peristaltic train of a given wave form. The nonlinear effects were further investigated for peristaltic pumping when an adverse pressure drop exists between two periodic sections (with the same pressure gradients), and for pumping by much more curvilinear peristaltic wall waves.

7.1. *The Reynolds number effects*

Profiles of the dimensionless longitudinal and lateral velocity components due to free pumping ($\mathscr{K} = 0$) at two different wave speeds are shown in figure 13. The solid curves are for $\mathscr{R} = 2{\cdot}25$ while the dashed ones are for $\mathscr{R} = 25{\cdot}1$. The former resemble those for a single-bolus flow at $\mathscr{R} = 2{\cdot}5$ (see figure 7), although a small Couette effect due to the forward longitudinal velocity component of the inextensible wall is absent for the case of purely transverse wall motion. Because of the reduction in channel spacing ($0{\cdot}208\lambda$ *vs.* $0{\cdot}131\lambda$), the maximum longitudinal velocity (which occurs on the axis near the plane of longitudinal symmetry) is increased over that of the single bolus from

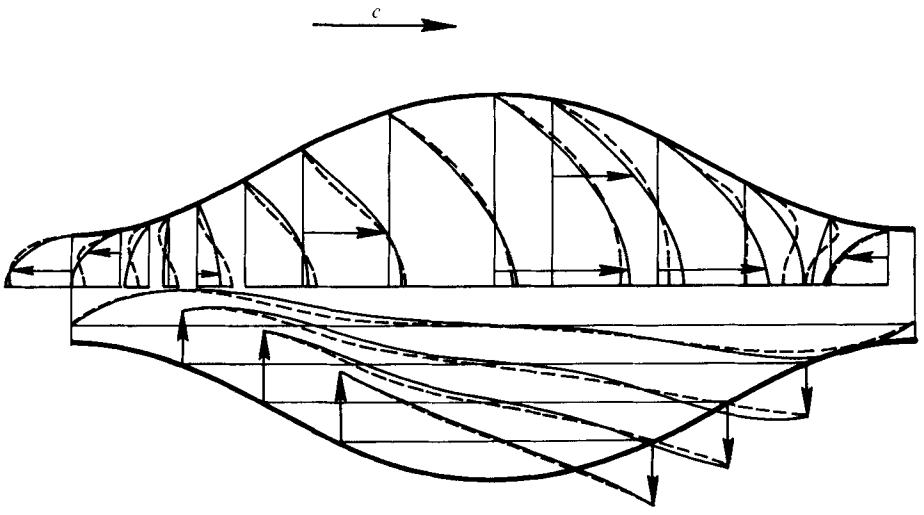

FIGURE 13. Effect of fluid inertia on the fixed-frame velocity profiles. Periodic elastic-wall wave; $A/\lambda = 0{\cdot}164$, $d/\lambda = 0{\cdot}131$, $\mathscr{K} = 0$. ——, $\mathscr{R} = 2{\cdot}25$; – – –, $\mathscr{R} = 25{\cdot}1$.

$0{\cdot}735c$ to $0{\cdot}938c$. The ratio of temporal mean discharge $\bar{Q}_F$ to $\mathscr{R}$ (at any section in the fixed co-ordinates) increases from 0·805 to 0·865. Because the dimensionless velocity components are in the form of a Reynolds number [refer to (11)], this temporal mean discharge can be expressed as

$$\bar{Q}_F = 2\int_0^{\beta_{\text{wall}}} U\,d\beta + \frac{2\mathscr{R}}{\lambda}\int_0^{\lambda} g(x)\,dx. \tag{22}$$

Velocity profiles for periodic flow at $\mathscr{R} = 25{\cdot}1$ are depicted by the dotted lines in figure 13. With this ten-fold increase in Reynolds number, the longitudinal velocity component near the wall becomes even larger in the leading half of the bolus but smaller in the trailing half. As one moves inwards towards the axis, this trend is seen to reverse. Similar phenomena were encountered by Jaffrin (1973) for small but finite Reynolds number and a vanishing ratio of wave amplitude to wavelength. The increase in $\bar{Q}_F$ with the Reynolds number for finite amplitudes shows the opposite trend from the small wave amplitude ($A \ll \lambda$) peristalsis studied by many investigators (Jaffrin & Shapiro 1971).

For $\mathscr{R} = 25{\cdot}1$ the lateral velocity component, which at the lower Reynolds number was nearly antisymmetrical about the bolus midsection, is now augmented in the wall region. An opposite effect (inward shift in lateral velocity) occurs near the highly curved segments of the leading and trailing edges of the wall. A further consequence of this ten-fold increase in the inertial effects is the increasing asymmetry of the shear stress (refer to figure 14) along the wall. The maximum wall shear stress is increased by a factor of 19, with the peak value occurring somewhat nearer to the leading edge.

An additional ten-fold increase in the relative inertial effects (see figure 15) to $\mathscr{R} = 251$ shows a marked flattening of the longitudinal velocity profiles which is somewhat suggestive of that observed for potential peristaltic flow (compare with figure 3). Although the maximum longitudinal velocity at $\mathscr{R} = 251$ falls to $0{\cdot}701c$, the pumping effectiveness is improved by another 10 % (with $\bar{Q}_F$ now equal to $0{\cdot}955\mathscr{R}$). The dimensionless shear rate at the wall increases even more rapidly, at some points

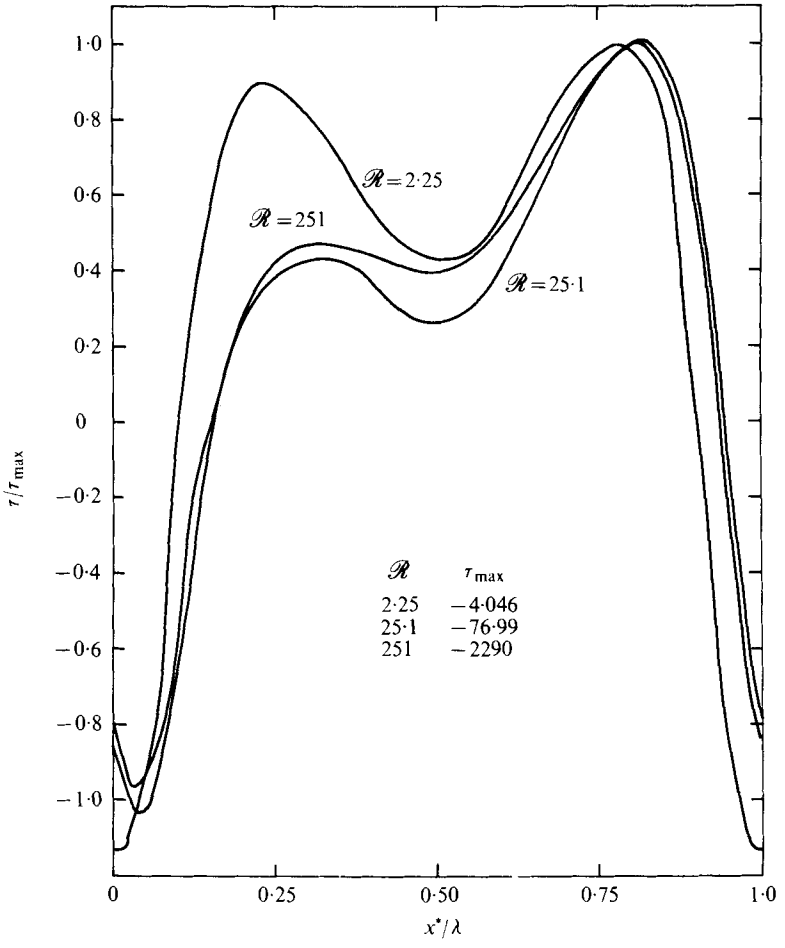

FIGURE 14. Tangential shear stress distribution along the wall for $A/\lambda = 0{\cdot}164$, $d/\lambda = 0{\cdot}131$, $\mathscr{K} = 0$.

to more than twice its value at $\mathscr{R} = 25{\cdot}1$, leading to augmentation of the peak shear stress by an additional factor of 30. This would indicate that strong enhancement of the inertial effects at the wall by increasing the peristaltic wave speed may not be a desirable means of increasing the flow rate of stress-sensitive fluids such as blood because of the possible damage to blood elements.

The effects of fluid inertia upon the pressures developed within a peristaltic bolus for the free-pumping end condition are depicted in figure 16. The maximum longitudinal pressure variations, observed to occur along the wall, are plotted for four different Reynolds numbers. Owing to the large wall curvature, the pressure also varies across lateral sections. With a moderate increase of from 2·25 to 25·1, the large difference between the two wall pressure extrema at $x^*/\lambda = 0{\cdot}15$ and 0·90 for the former case diminishes, although a vestige of the longitudinal asymmetry in the distribution can still be detected. For a further inertial increase to $\mathscr{R} = 251$, the wall pressure distribution tends monotonically towards that of the potential-flow case. The present results imply that for the same ambient pressure (outside the channel) the maximum magni-

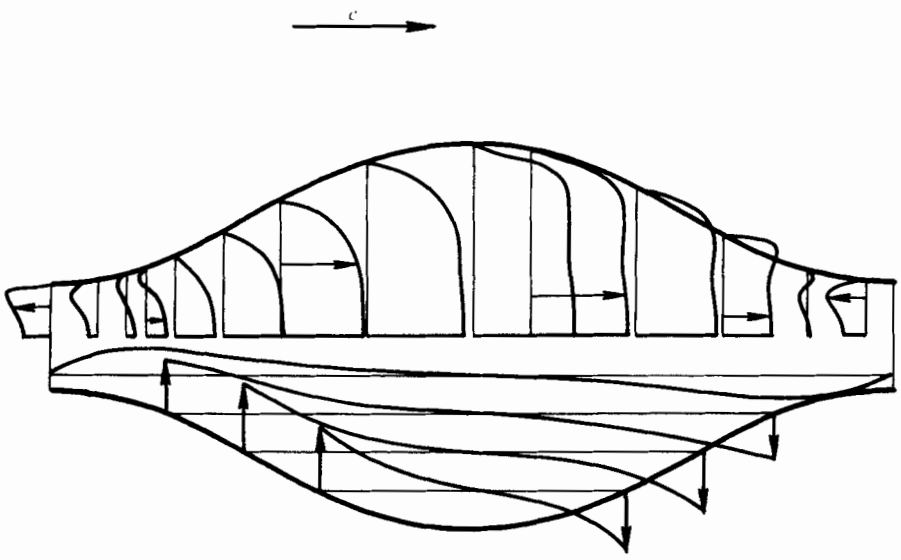

FIGURE 15. Fixed-frame velocity profiles for the pumping pattern of figure 13, with $\mathscr{R} = 251$.

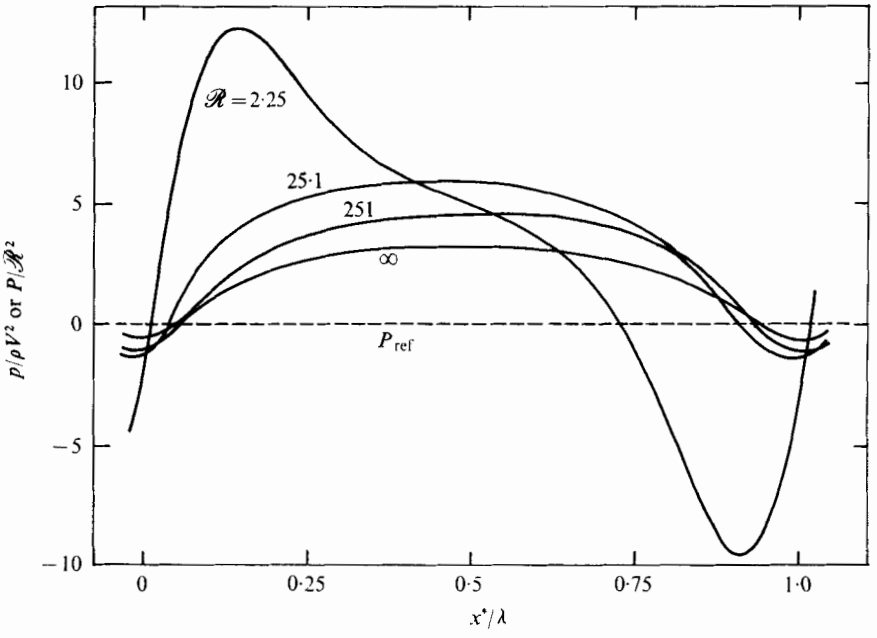

FIGURE 16. The effect of fluid inertia on the pressure distribution along the wall. Parameter values for $\mathscr{R} = 2{\cdot}25$, 25·1 and 251 correspond to the flows in figures 13 and 15. For $\mathscr{R} = \infty$, $\phi_b - \phi_b = 8{\cdot}0$.

tude of the dimensionless applied force of contraction and dilatation necessary to propagate a prescribed peristaltic wave form will reduce as the Reynolds number increases. Furthermore, the trend towards a more symmetrical distribution of the wall pressure correlates with the decreasing viscous energy dissipation (which tends to zero as μ vanishes): a greater portion of the contractile work done by pressure (in the trailing half of the wall) is recoverable as dilatational pressure work done by the wall

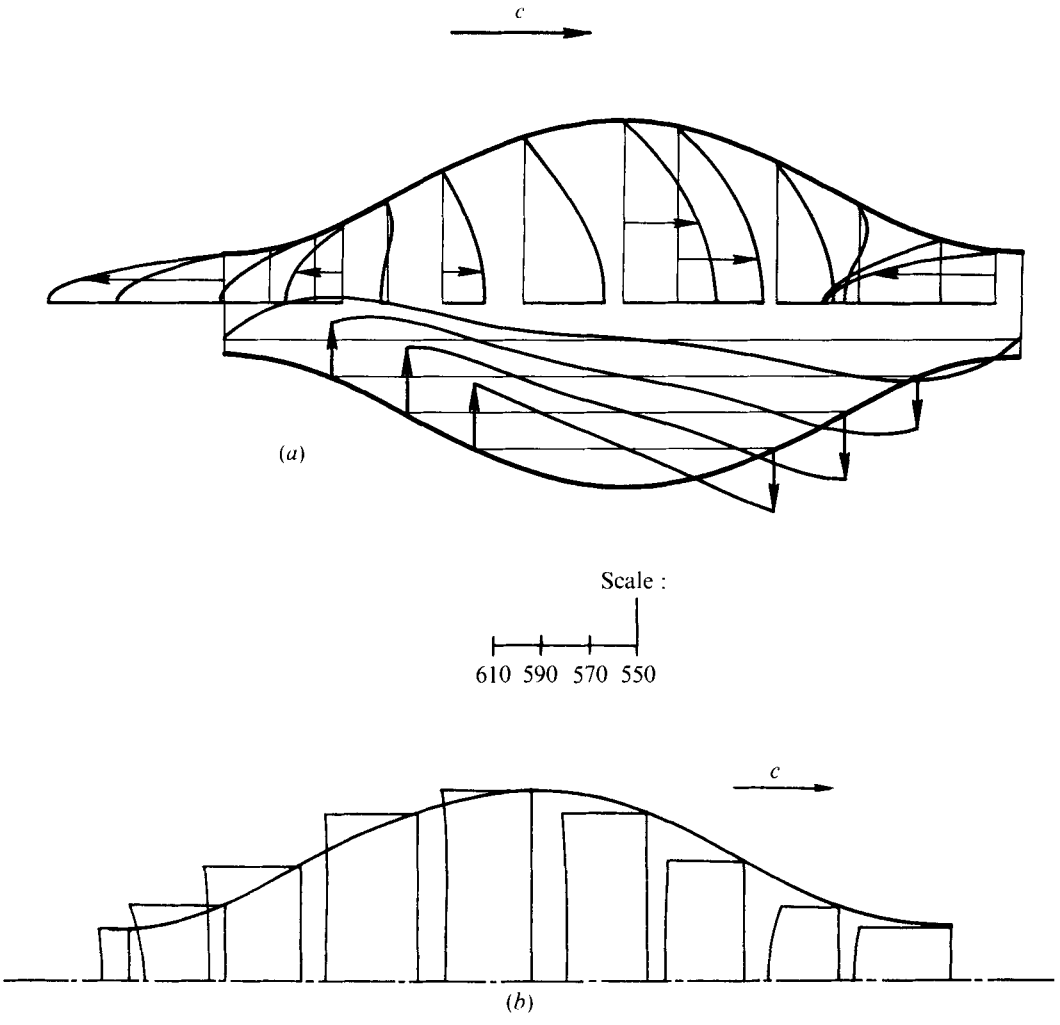

FIGURE 17. (*a*) Fixed-frame velocity profiles and (*b*) pressure profiles for pumping against a mild adverse pressure gradient; $A/\lambda = 0{\cdot}164$, $d/\lambda = 0{\cdot}131$. $\mathscr{R} = 2{\cdot}25$, $\mathscr{H} = -39{\cdot}25$, periodic wall wave with elastic-wall boundary conditions (*b*).

in the leading half of the wave. However, to propagate the same wave form at low Reynolds numbers (e.g. 2·25), it is necessary to supply additional energy from the contracting part of the wall to a portion of the dilating wall segment.

7.2. *The Kármán number effects*

Velocity profiles for pumping against an adverse pressure gradient by peristalsis are shown in figure 17 for a Kármán number of $-39{\cdot}25$. The magnitude of this imposed Kármán number corresponds to a net pressure drop equal to the largest pressure differential observed within the bolus for the free-pumping case (see solid lines in figure 13). The wall shear and the longitudinal velocity component in most parts of the dilating bolus decrease, while large shearing stresses are developed at the neck segments because of the three-fold increase in retrograde velocity. These alterations, which are

caused by the adverse $\mathscr{K}$, result in an increase in the lateral velocity; clearly, the 'Poiseuille-flow component' must diverge laterally and then converge to accommodate the spatially varying channel width. The effects of the adverse pressure differential on the pressure distribution can be seen by comparing the results shown in figure 17(*b*) with those in figure 4. A continuous increase in the adverse $\mathscr{K}$ would eventually lead to flow separation in the diverging section of the wave unless the intensity of peristalsis were augmented. It can be seen that, when the opposing effects of a pressure drop and peristaltic wall motion are of approximately equal magnitude, a situation which arises (for moderate channel spacings) when pumping against a relatively mild pressure gradient, the effectiveness of fluid transport by peristalsis is markedly reduced. In the present example, the adverse pressure drop resulted in a 62 % decrease in the temporal-mean discharge in the fixed frame, from 0·805 to 0·306. Comparable changes in the pumping effectiveness ensue when the effects of a pressure drop and wall peristalsis are complementary.

7.3. *The effects of large wall curvature*

Computational and experimental flow patterns viewed from the moving reference frame for a peristaltic flow in which the effects of large wall curvature dominate those of finite fluid inertia are shown in figure 18 (plate 1). The numerically obtained streamlines (upper half) agree well with the experimentally visualized bubble path lines (lower half) in their delineation of the size and location of the secondary flow vortices. The path-line tracings, in which the ripples were caused by vibrations of the camera, reflect higher velocities near the wall. As was pointed out in the linearized analyses of Shapiro *et al.* (1969), Tong & Vawter (1972) and Jaffrin (1973), the occurrence of a moving-reference-frame stagnation point along the axis is indicative of a splitting of the streamline $\Psi = 0$ from the axis. The trapped fluid enclosed by this split streamline must then move forwards with a net advance velocity equal to the wave speed. Depending upon the pressure drop, an appreciable portion of the fluid within the bolus may be trapped even when the channel is not fully occluded. In this free-pumping case ($\mathscr{K} = 0$), the relative trapping intensity, defined as the ratio of the maximum magnitude of the stream function within the secondary vortices to that along the channel walls, is calculated to be 22·3 %. The trend of decreasing trapping intensity reported by Jaffrin (1973) for a small increase in inertia at a zero ratio of wave amplitude to wavelength is also noted in the present study for a large increase in inertia at a finite amplitude ratio. In the limiting case of potential flow, the maximum backward velocity in the moving frame occurs along the bolus axis rather than at the wall, indicating that, at very large Reynolds number or in the absence of viscous effects, trapping in the core is unlikely to occur unless the channel is almost fully occluded.

As can be seen from the contour plot in figure 19(*a*), a large adverse pressure drop occurs across the highly constricted neck region of the bolus. For the free-pumping case, this pressure drop is balanced by a gradual increase in pressure from the leading edge to the trailing edge. The shearing stress peaks along the wall at the bolus necks (figure 19*b*); its distribution exhibits much greater longitudinal symmetry about the section $x^* = \frac{1}{2}\lambda$ than was observed for a smaller wave amplitude at a comparable $\mathscr{R}$ (refer to figure 19*b*). Figure 19(*c*) confirms the intuitive expectation that the secondary vortices characteristic of trapping have an insignificant energy dissipation rate compared with that observed along the axis on either side of the highly occluded region. The dynamic characteristics of this pair of trapping vortices are similar to those of

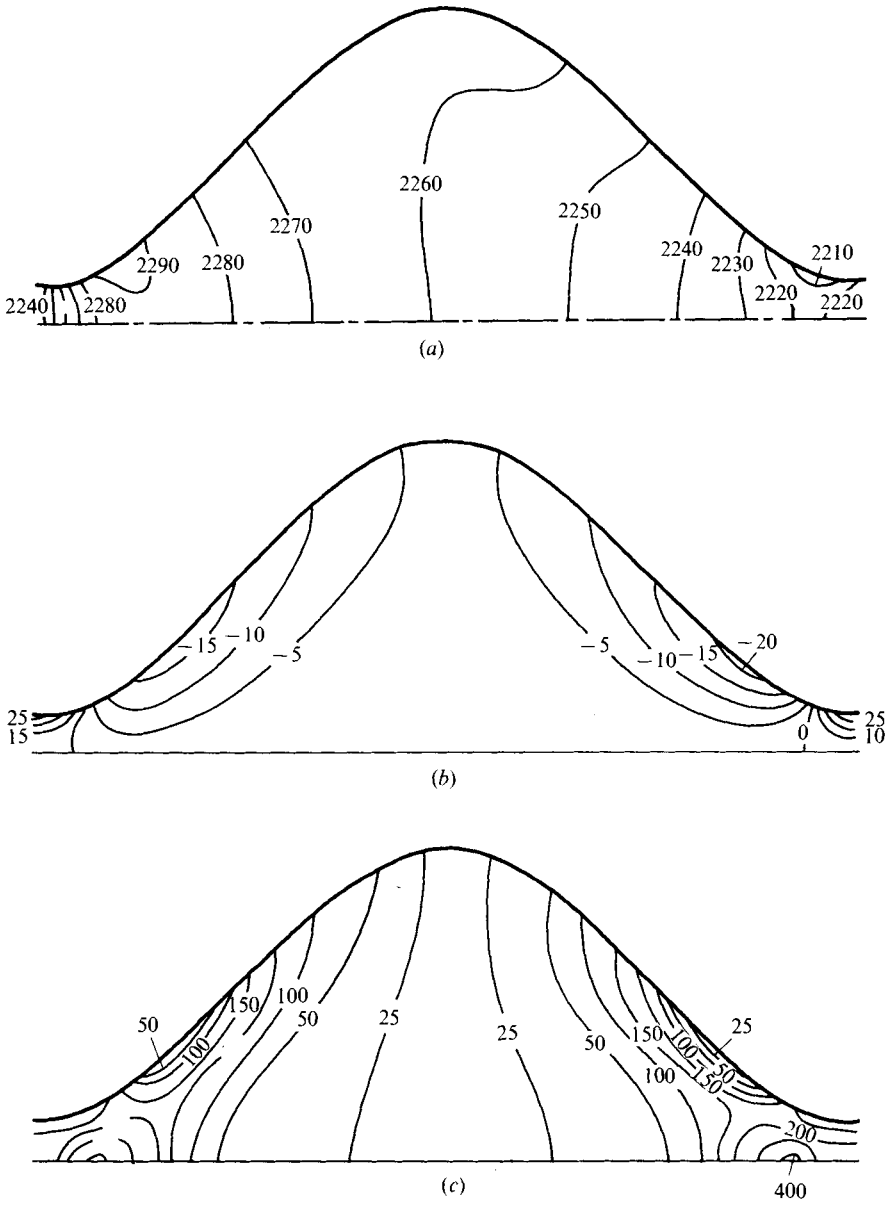

FIGURE 19. Contours of (*a*) pressure, (*b*) shearing stress and (*c*) energy dissipation for the flow in figure 18.

steady laminar vortices in a conduit expansion (Macagno & Hung 1967*a*, *b*); for both cases, the role of vortices is to guide the longitudinal flow through the channel transition without a large expenditure of energy within the vortices themselves. Unlike the boundary-layer separation, however, the peristalsis propels the captive vortices along the centre-line of the channel.

NSF Grant GK-31514 to T.K.H. and support to T.D.B. under NIH Training Grant GMO-1455 during part of the investigation are acknowledged. The authors would like to express their appreciation to Mrs Diana Montgomery for her secretarial assistance. Excellent computational facilities were provided by the Computation Centers of Carnegie-Mellon University and the University of Pittsburgh.

REFERENCES

BROWN, C. H., LEMUTH, R. F., HELLUMS, J. D., LEVERETT, L. G. & ALFREY, C. P. 1975 Response of human platelets to shear stress. *Trans. Am. Soc. Artif. Int. Organs* **21**, 35–38.

BROWN, T. D. 1976 Computational and experimental studies of two-dimensional nonlinear peristaltic pumping. Ph.D. thesis, Carnegie-Mellon University.

ECKSTEIN, E. 1970 Experimental and theoretical pressure studies of peristaltic pumping. S.M. thesis, Massachusetts Institute of Technology.

FUNG, Y. C. & YIH, C. S. 1968 Peristaltic transport. *J. Appl. Mech.* **35**, 669–675.

HANIN, M. 1968 The flow through a channel due to transversely oscillating walls. *Israel J. Tech.* **6**, 67–71.

HARLOW, F. H. & WELCH, J. E. 1965 Numerical calculation of viscous incompressible flow of fluid with free surface. *Phys. Fluids.* **8**, 2182–2189.

HUNG, T. C., HOCHMUCH, R. M., JOIST, J. H. & SUTERA, S. P. 1976 Shear-induced aggregation and lysis of platelets. *Trans. Am. Soc. Artif. Int. Organs* **22**, 285–291.

HUNG, T.-K. 1970 Vortices in pulsatile flows. *Proc. 5th Int. Cong. Rheol.* vol. 2, pp. 115–127.

HUNG, T.-K. & BROWN, T. D. 1976 Solid-particle motion in two-dimensional persistaltic flows. *J. Fluid Mech.* **73**, 77–97.

HUNG, T.-K. & BROWN, T. D. 1977 An implicit finite-difference method for solving the Navier–Stokes equation using orthogonal curvilinear coordinates. *J. Comp. Phys.* **23**, 343–363.

JAFFRIN, M. Y. 1973 Inertia and streamline curvature effects on peristaltic pumping. *Int. J. Engng Sci.* **11**, 681–699.

JAFFRIN, M. Y. & MEGINNISS, J. R. 1971 The hydrodynamics of roller pumps and their implication to hemolysis. *M.I.T. Fluid Mech. Lab. Publ.* no. 71–1.

JAFFRIN, M. Y. & SHAPIRO, A. H. 1971 Peristaltic pumping. *Ann. Rev. Fluid Mech.* **3**, 13–35.

MACAGNO, E. O. & HUNG, T.-K. 1967*a* Pressure, Bernouilli sum and momentum and energy relations in a laminar zone of separation. *Phys. Fluids* **10**, 78–92.

MACAGNO, E. O. & HUNG, T.-K. 1967*b* Computational and experimental study of a captive annular eddy. *J. Fluid Mech.* **28**, 43–64.

MITTRA, T. K. & PRASAD, S. N. 1973 On the influence of wall properties and Poiseuille flow in peristalsis. *J. Biomech.* **6**, 681–693.

NEGRIN, M. P., SHACK, W. J. & LARDNER, T. J. 1974 A note on peristaltic pumping. *J. Appl. Mech.* **96**, 520–521

SHAPIRO, A. H., JAFFRIN, M. Y. & WEINBERG, S. L. 1969 Peristaltic pumping with long wavelengths at low Reynolds number. *J. Fluid Mech.* **37**, 799–825.

TAYLOR, G. I. 1951 Analysis of the swimming of microscopic organisms. *Proc. Roy. Soc.* A **209**, 447–461.

THOM, A. & APELT, C. J. 1961 *Field Computations in Engineering and Physics.* Van Nostrand.

TONG, P. & VAWTER, D. 1972 An analysis of peristaltic pumping. *J. Appl. Mech.* **39**, 857–862.

WELCH, J. E., HARLOW, F. H., SHANNON, J. P. & DALY, B. J. 1966 The MAC method: a computing technique for solving viscous, incompressible, transient fluid-flow problems involving free surfaces. *Los Alamos Sci. Lab. Rep.* LA-3425.

YIN, F. C. P. & FUNG, Y. C. 1971 Comparison of theory and experiment in peristaltic transport. *J. Fluid Mech.* **47**, 93–113.

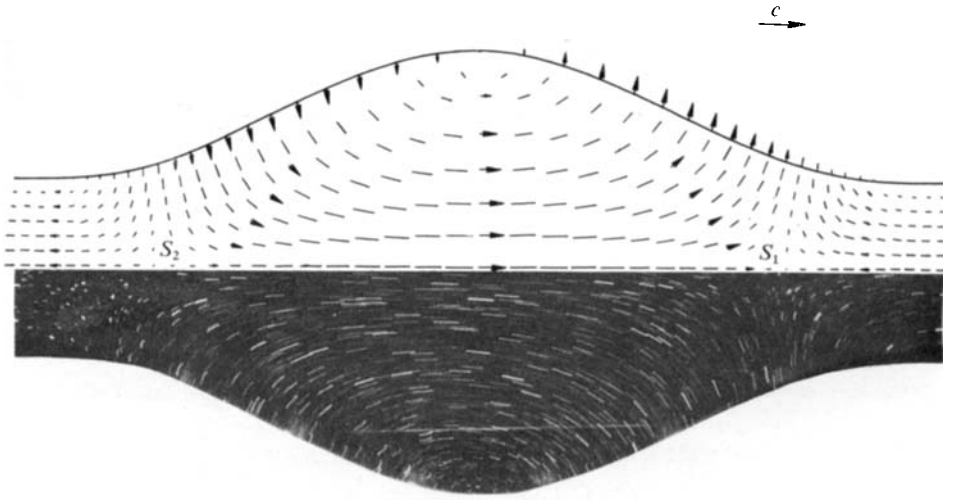

FIGURE 8. Comparison of computationally obtained (upper) and experimentally observed (lower) flow fields. $A/\lambda = 0{\cdot}164$, $d/\lambda = 0{\cdot}208$, $\mathscr{R} = 2{\cdot}36$, $\mathscr{K} = 0$.

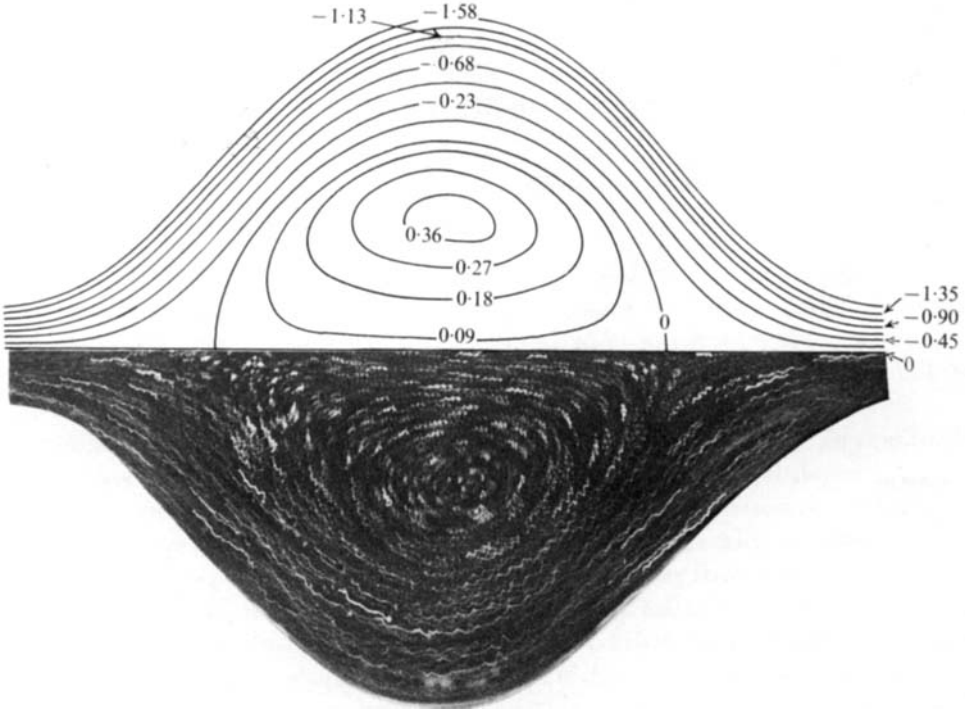

FIGURE 18. Moving-frame streamlines (upper) and bubble path lines (lower) for the trapping condition. $A/\lambda = 0{\cdot}328$, $d/\lambda = 0{\cdot}0983$, $\mathscr{R} = 4{\cdot}75$, $\mathscr{K} = 0$, periodic wave with elastic-wall boundary conditions.